Substantial Improvement of Operating Stability by Strengthening Metal-Halogen Bonds in Halide Perovskites

Xi Chen, Zhiguo Sun, Bo Cai, Xiaoming Li, Shihua Zhang, Di Fu, Yousheng Zou, Zhiyong Fan, and Haibo Zeng*

Solution-processed lead halide perovskites (LHPs) hold great promise for low-cost high-performance solar cells and light-emitting devices, but they also suffer from a serious operating instability problem due to the ionic migration and lattice decomposition driven by strong electric fields. Here, considerably suppressed ionic migration and enhanced lattice stability in LHPs with partial substitution of Pb with 3d transition metal (TM: Mn and Ni) are reported. It is experimentally shown that the energy barrier for ionic migration in $CsPbBr_3$ can be increased fourfold by Mn and Ni substitution, even with a small doping level (<4%). However, post-TM Zn and non-TM Bi incorporations are less efficient in suppressing ionic migration. The theoretical results reveal that Ni and Mn ions with partially filled 3d orbitals can passivate the active lone-pair electron of surrounding Pb-Br octahedrons via a coordination effect and reduce the Pb 6s-Br 4p antibonding states, resulting in long-range lattice stabilization and suppressed ionic migration. The Ni incorporation strategy in mixed-halogen $CsPbBr_{1.5}I_{1.5}$ is further demonstrated, for which the field-driven halogen segregation is significantly mitigated and the associated emission color variation is reduced sixfold. This study paves the way for improving the operating stability in LHP-based optoelectronic and electronic devices.

1. Introduction

The superiority of lead halide perovskite (LHP) semiconductors, which emerged in recent years, over conventional silicon and gallium arsenide crystals for optoelectronic applications such as solar cell and light emitting diode devices lies in their low-temperature solution processability and high defect tolerance.[1] The former enables low-cost and scalable device fabrication, but it usually introduces dense lattice defects. The latter ensures efficient photon-electron interconversion despite the dense defects,

X. Chen, Z. Sun, B. Cai, X. Li, S. Zhang, D. Fu, Y. Zou, H. Zeng
MIIT Key Laboratory of Advanced Display Materials
and Devices, School of Materials Science and Engineering
Nanjing University of Science and Technology
Nanjing 210094, China
E-mail: zeng.haibo@njust.edu.cn
Z. Fan
Department of Electronic and Computer Engineering
The Hong Kong University of Science and Technology
Clear Water Bay, Kowloon, Hong Kong SAR 999077, China

due to the fact that the major defects in LHP lattices, that is, the atomic vacancies, are in shallow energy levels in bands.[2] Unfortunately, the presence of abundant atomic vacancies in turn facilitates vacancy-mediated ionic migration under electrical loads and/or optical illumination, which has tremendous impacts on the intrinsic optoelectronic and electronic properties of LHPs. It has been shown that field-driven ionic migration can induce ionic segregation and lead to the formation of vacancy-rich and halogen-rich domains, which decomposes the LHP lattices, alters the bandgap, blocks the charge carrier extraction, and consequently degrades the device performance, usually on a timescale of seconds to hours.[3–8] Additionally, ionic migration has been shown to be a major cause of the current-voltage hysteresis in LHP-based solar cells,[9–11] which imposes challenges on stabilizing the power conversion efficiency. Therefore, despite the fact that the efficiency of LHP-based solar cells and light emitting devices has now achieved impressive values above 20%,[12–14] the demand for rapid commercialization has come into conflict with the operating instability caused by field-driven ionic migration.

Methods such as reducing the structural dimensionality,[15] inserting ion-transport-blocking layers,[6,16] passivating nanocrystal/film surfaces,[17,18] and enlarging grain size[19] have been sought to suppress the ionic migration and improve the operating stability in solution-processed LHPs. Nonetheless, there is still a strong requirement to further enhance the stability of LHPs for commercial use. Another well-demonstrated method is composition engineering. It has been shown that entirely or partially replacing polar monovalent cations in LHPs (e.g., $CH_3NH_3^+$ in $CH_3NH_3PbI_3$) with less polar or nonpolar monovalent cations (e.g., $HC(NH_2)_2^+$ or Cs^+) can increase the energy barrier of ionic migration and weaken the current-voltage hysteresis because of the reduced vacancy-dipole interaction.[20–24] Recently, the doping of the Pb site with Mn, Ni, Zn, Cd, Co, or Sr was found to improve the power conversion efficiency, the photoluminescence quantum yield (PLQY), and the stability of solution-processed LHPs,[25–35] demonstrating that Pb site engineering is an attractive way to fabricate high-performance LHP devices. However, in those studies, the stability improvement induced by the Pb site doping was mainly limited to the phase transition

or ambient degradation. The effect of the Pb site doping on the field-driven ionic migration has been less studied. Moreover, the mechanisms for the improvements have commonly been attributed to the optimization of lattice ordering, the relaxation of lattice strain, or the reduction of defect states due to the exotic ion incorporation. The influence on the chemical bonding/antibonding states of the Pb-halogen bonds, which are directly linked to the lattice stability and the ionic migration kinetics, is largely unknown. Addressing these issues will improve the existing understanding of doping-related stability enhancement and provide a perspective for further optimizing the operating durability in LHP-based optoelectronic and electronic devices.

In this research, with a combination of experiments and first-principles calculations, we demonstrate that the partial substitution of Pb with a 3d transition metal (TM) whose 3d orbital is partially filled can significantly tune the ionic migration kinetics and enhance the lattice stability of LHPs with respect to external stress. The experimental results show a fourfold increase of the ionic migration barrier in Ni- or Mn-doped $CsPbBr_3$ and a sixfold reduction of the field-driven emission color variation in Ni-incorporated mixed-halide $CsPbBr_{1.5}I_{1.5}$ because of greatly suppressed halogen segregation. However, post-TM Zn with fully-filled 3d orbital and non-TM Bi incorporations are less efficient in suppressing the ionic migration. The doping-induced modulation of the electronic structures is investigated using first-principles calculations to analyze the covalent bonding and antibonding states in the metal-halogen bonds. The theoretical calculation results suggest that the coupling between the partially-filled 3d orbital and the Pb 6s-Br 4p antibonding states is key to the stabilization of the whole lattice and thus the suppressed ionic migration.

2. Results and Discussion

2.1. Doping Characterization

We synthesize metal ion-incorporated $CsPbBr_3$ quantum dots via a solution-processed hot-injection method. The samples are abbreviated as $CsPb_{1-x}M_xBr_3$, where M represents TM Mn and Ni, post-TM Zn, and non-TM Bi, and x is the real molar ratio of the metal ion relative to Pb ($x = 0$ represents pure $CsPbBr_3$). Inductively coupled plasma mass spectroscopy is used to quantify the x values (Table S1, Supporting Information). To confirm the successful incorporation of the dopants into the $CsPbBr_3$ lattice, we investigate the structural and optical properties of $CsPb_{1-x}Ni_xBr_3$ quantum dots as an example. **Figure 1**a,b shows the low-magnification and high-resolution transmission electron microscopy (TEM) images of $CsPb_{1-x}Ni_xBr_3$ quantum dots with $x = 0$ and 0.0275. The quantum dots show a typical square morphology with a mean edge length of 12.39 nm for $x = 0$ and 12.15 nm for $x = 0.0275$, suggesting that the Ni incorporation has less influence on the size of the quantum dots. Clear lattice fringes are observed from the high-resolution TEM images, indicating that our samples are well crystallized. The fringe spacing determined by using fast Fourier transform patterns is found to be ≈0.29 nm for both samples, which are assigned to the (200) plane. Figure 1c shows the powder X-ray diffraction (XRD) patterns of the $CsPb_{1-x}Ni_xBr_3$ quantum dots. All of the samples can be indexed as cubic-phase $CsPbBr_3$. A close look

at the XRD patterns near $2\theta = 30°$ reveals that the Bragg angle θ shifts to higher values with increasing x, suggesting that the lattice has contracted. Since Ni^{2+} ion has a smaller Shannon radius than Pb^{2+} (0.69 Å versus 1.19 Å), the lattice contraction is evidence of the successful incorporation of Ni into the Pb sites. The elemental mappings obtained with energy-dispersive X-ray spectroscopy also suggest the presence of Ni in the $CsPbBr_3$ lattice (Figure S1, Supporting Information). This is further corroborated by the X-ray absorption fine structure (XAFS) spectra measurements shown in Figure 1d, since XAFS is a powerful technique for examining the coordination environment of the absorbing atoms.[36] The Ni K-edge absorption spectrum of the $CsPb_{1-x}Ni_xBr_3$ with $x = 0.0275$ shows a similar rising edge to that of the referenced NiO, indicating that the Ni dopants have +2 valence, as expected. Moreover, in contrast to the referenced elementary Ni foil, the Ni K-edge absorption spectrum of the Ni-incorporated $CsPbBr_3$ is more akin to that of the referenced NiO. Both spectra show very weak pre-edge features, similar white line absorptions, and identical white line resonance peaks (≈8348.6 eV). These characteristics indicate that the coordination environment of Ni in $CsPbBr_3$ is similar to that in NiO,[29,37] that is, the Ni in $CsPbBr_3$ is octahedrally coordinated, or rather, in the Pb^{2+} sites.

The effects of Ni incorporation on the photoluminescence (PL) properties of the $CsPb_{1-x}Ni_xBr_3$ quantum dots are shown in Figure 1e. We observe a slight blue-shift of the bandgap with the increasing x, consistent with previously reported results due to small ion doping-induced lattice contraction.[27–30,38] Figure 1f shows the PLQY of $CsPb_{1-x}Ni_xBr_3$ quantum dots, which suggests that the PLQY is maintained at around ≈82% regardless of the x values. Both the PL and PLQY results demonstrate that the Ni incorporation has no detrimental effects on the optical performances of the $CsPbBr_3$. The successful incorporation of Mn and Zn into the $CsPbBr_3$ lattice is also confirmed by the powder XRD and the optical measurements (Figure S2, Supporting Information).

2.2. Substantial Suppression of Ionic Migration

We measure the transport properties of $CsPb_{1-x}M_xBr_3$ as a function of temperature (T) to extract the ionic migration activation energy ($E_{a,i}$). We employ a lateral structure device that is composed of two Cr/Au electrodes with a distance of 20 μm covered by $CsPb_{1-x}M_xBr_3$ quantum dots, as sketched in Figure S3, Supporting Information. An external electric field with a magnitude of 15 V is applied between the two electrodes to initiate the ionic migration, and the electric current is detected under dark conditions. The measurement is carried out in a vacuum environment of ≈2×10^{-2} Pa to rule out degradation pathways induced by oxygen and moisture in air. We assume that only ionic and electronic currents (I_i and I_e) exist and that the ionic transport and the electronic transport in the $CsPbBr_3$ are governed by a vacancy mechanism[39,40] and a thermally activated polaron hopping mechanism,[41,42] respectively. In this regard, according to the principle of a parallel circuit, the expression for the detected total electric current (I_{total}) is given by

$$I_{total} = I_i + I_e \tag{1}$$

**ADVANCED
SCIENCE NEWS**

www.advancedsciencenews.com

**ADVANCED
FUNCTIONAL
MATERIALS**

www.afm-journal.de
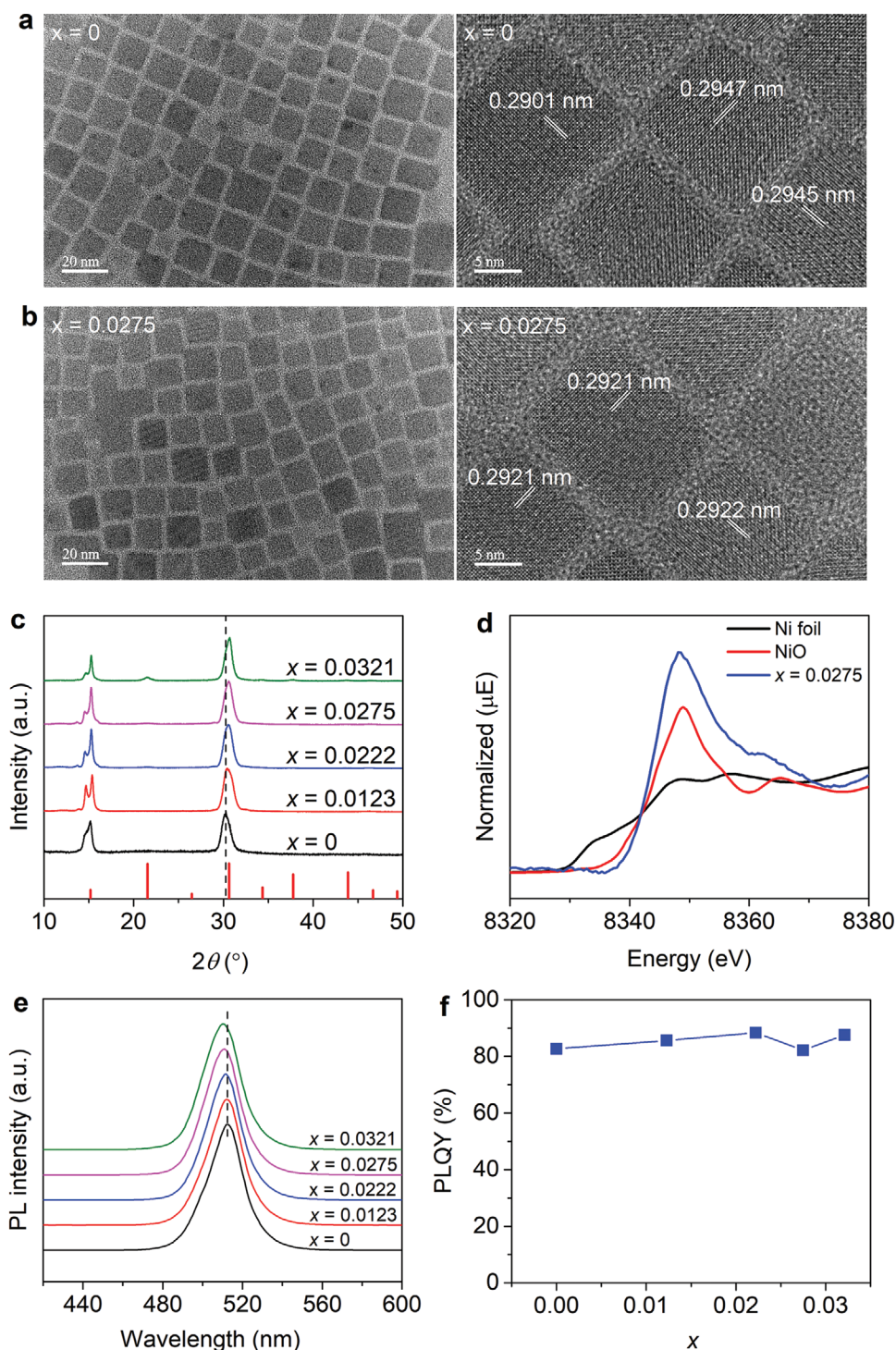
Figure 1. Structure and optical properties of $CsPb_{1-x}Ni_xBr_3$ quantum dots. Low-magnification and high-resolution TEM images of $CsPb_{1-x}Ni_xBr_3$: a) $x = 0$ and b) $x = 0.0275$. c) Powder XRD patterns of $CsPb_{1-x}Ni_xBr_3$. d) Ni K-edge XAFS spectra of Ni foil, NiO, and $CsPb_{1-x}Ni_xBr_3$ with $x = 0.0275$. e) PL spectra. f) PLQY of $CsPb_{1-x}Ni_xBr_3$.

where I_i and I_e can be determined with the standard Arrhenius model:

$$I_i = \frac{A_i}{T}\exp\left(-\frac{E_{a,i}}{k_BT}\right) \tag{2}$$

$$I_e = \frac{A_e}{T}\exp\left(-\frac{E_{a,e}}{k_BT}\right) \tag{3}$$

where A_i and A_e are the pre-exponential factors, $E_{a,e}$ is the activation energy for electronic polaron hopping, and k_B is the

ADVANCED
SCIENCE NEWS
www.advancedsciencenews.com

ADVANCED
FUNCTIONAL
MATERIALS
www.afm-journal.de
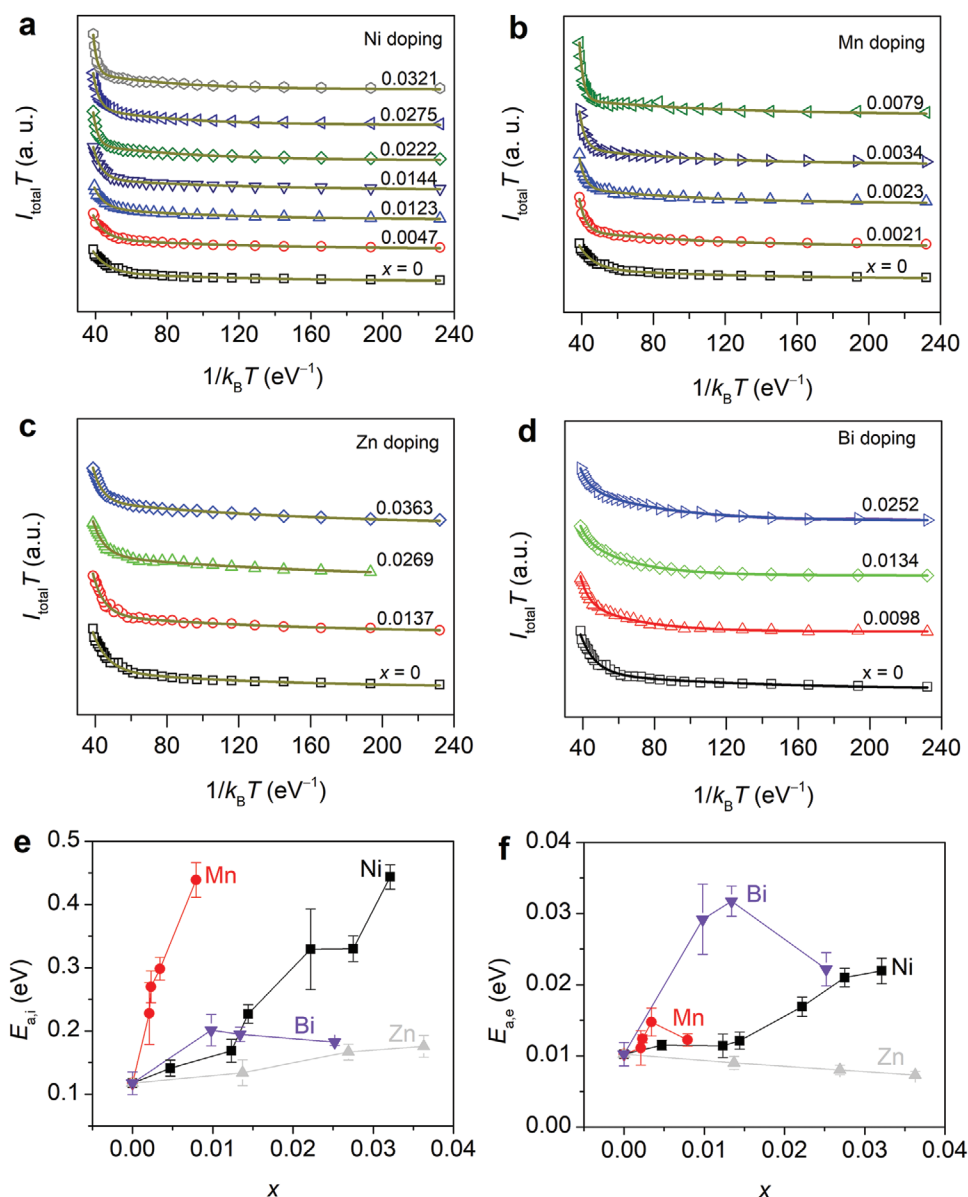
Figure 2. Electronic and ionic migration energy barriers. (a,b,c, and d) show the $I_{total}T$ versus $1/k_BT$ curves measured from lateral CsPbBr$_3$ devices with Ni, Mn, Zn, and Bi doping, respectively. The solid lines represent the fitting curves using Equation (4). (e) and (f) display the fitting results for $E_{a,i}$ and $E_{a,e}$ as a function of x. Error bars represent the standard errors estimated by measuring three lateral devices for each sample.

Boltzmann constant. With combination and transformation, we obtain

$$I_{total}T = A_e \exp\left(-\frac{E_{a,e}}{k_BT}\right) + A_i \exp\left(-\frac{E_{a,i}}{k_BT}\right) \quad (4)$$

It is evident that the $E_{a,i}$ and $E_{a,e}$ values can be extracted by fitting the $I_{total}T$ versus $1/k_BT$ curves using Equation (4).

Figure 2a–d plots the $I_{total}T$ versus $1/k_BT$ curves measured in the CsPb$_{1-x}$Ni$_x$Br$_3$, CsPb$_{1-x}$Mn$_x$Br$_3$, CsPb$_{1-x}$Zn$_x$Br$_3$, and CsPb$_{1-x}$Bi$_x$Br$_3$ devices, respectively. Two distinct regions are observed in these curves. In the $1/k_BT > 55$ eV^{-1} ($T < 210$ K) regime, the $I_{total}T$ increases very slowly with the decreasing

$1/k_BT$, indicating that in this region, the I_{total} is dominated by the electronic transport due to suppressed ionic migration at low T. In the $1/k_BT < 55$ eV^{-1} ($T > 210$ K) regime, the $I_{total}T$ exhibits a sharp increase with the decreasing $1/k_BT$, reflecting a significant contribution of the ionic transport to I_{total} because of thermally activated ionic migration. All the curves can be well fitted using Equation (4). The fitting results for $E_{a,i}$ are shown in Figure 2e. The $E_{a,i}$ is 0.117 eV in the undoped CsPbBr$_3$, and it increases to 0.443 eV with $x = 0.0321$ Ni incorporation and to 0.439 eV with $x = 0.0079$ Mn incorporation. The $E_{a,i}$ enhancement indicates that the ionic migration is greatly suppressed by the TM incorporation. However, such remarkable enhancement of $E_{a,i}$ is not

observed in Zn and Bi doping. The $E_{a,i}$ for Zn doping shows a slight increase to 0.175 eV at $x = 0.0363$. The $E_{a,i}$ for Bi doping initially increases to 0.201 eV at $x = 0.0098$, and then decreases to 0.182 eV at $x = 0.0252$. Nonetheless, the $E_{a,i}$ variation in the Zn and Bi doping cases is within the margin of error when compared with the undoped case. Therefore, we are of the view that the Zn and Bi doping are less efficient in suppressing ionic migration. The fitting results for $E_{a,e}$ are shown in Figure 2f. It is found that the $E_{a,e}$ increases with Ni doping and decreases with Zn doping, and it passes through a peak for Mn and Bi doping.

The $E_{a,i}$ values for Ni and Mn incorporation is comparable to previously reported ones with Cs-site doping.[23] It is worth noting that even if the Mn has a much smaller doping concentration than the Ni, the Mn incorporation can enhance the $E_{a,i}$ to the value close to that with the Ni incorporation, indicating that the Mn possesses a much higher efficiency in suppressing ionic migration. Using different Mn precursors or adopting a halide exchange-driven cation exchange method may help to optimize the Mn doping level,[43] which may further enhance the $E_{a,i}$.

2.3. Metal-Halogen Bonding Modulation Mechanism

To clarify the underlying mechanisms for the suppressed ionic migration due to TM incorporation, we perform a first-principles density functional theory (DFT) calculation study. We focus on halogen vacancy-mediated ionic migration along the octahedron edges because halogen vacancy is the dominant defect in solution-processed LHPs.[2,40] **Figure 3**a shows the top view of the (001) plane of a $3 \times 3 \times 3$ cubic $CsPbBr_3$ supercell that contains one Ni^{2+} ion, corresponding to a doping level of 3.7%. Three crystallography nonequivalent Br vacancies (V_{Br}), which are marked as P1, P2, and P3, are created to model the vacancy migration progress. The calculated energy profile for the V_{Br} hopping between P1, P2, and P3, including the energies at the ground state (E_{gs}, relative to P1) and at the transition state (E_{ts}), is sketched in Figure 3b. The pure $CsPbBr_3$ has equal E_{gs} regardless of the V_{Br} position, since the three V_{Br} positions in this case are completely equivalent in crystallography and thus in energy. The $E_{a,i}$, defined as the difference between E_{gs} and E_{ts}, is determined to be 0.26 eV in the pure $CsPbBr_3$. When Ni is introduced, however, the E_{gs} and E_{ts} values become highly
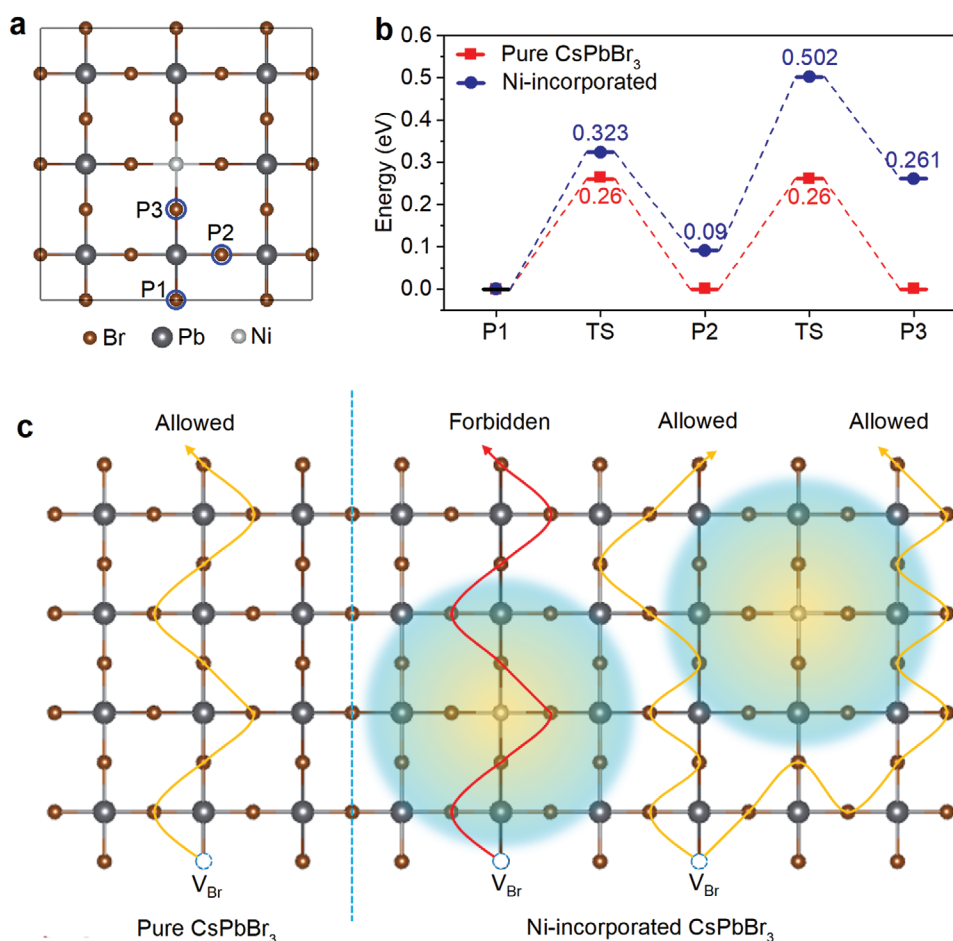
Figure 3. Ionic migration modeling. a) Top view of the (001) plane in a $3 \times 3 \times 3$ cubic-phase $CsPbBr_3$ supercell used for the DFT calculations. The Ni^{2+} ion is located at the center of the supercell. To model the ionic migration process, V_{Br} is created at three kinds of positions with different distances to the Ni^{2+} ion, that is, P1, P2, and P3. b) Ni incorporation effect on the energy profiles for V_{Br} located at the ground state (i.e., at P1, P2, and P3) and the transition state (TS). c) Illustration of the repelling effect of Ni on the moving V_{Br}. Compared with the pure $CsPbBr_3$ case, the repelling effect reduces the ionic migration channels and lengthens the migration path.

dependent on the V_{Br} position. The E_{gs} values at P2 and P3 are 0.09 and 0.261 eV higher than that at P1, respectively. The $E_{a,i}$ values for the V_{Br} hopping from P1 to P2 and from P2 to P3 are 0.318 and 0.408 eV, respectively, both of which are higher than the value in pure CsPbBr$_3$. The elevated E_{gs} with the enhanced $E_{a,i}$ suggests that the V_{Br} hopping toward the Ni^{2+} ion is forbidden in energy. This behavior may give rise to a repulsion effect on the migrating V_{Br}, as depicted in Figure 3c, which reduces the V_{Br} migration channels and increases the V_{Br} migration length, explaining the $E_{a,i}$ enhancement in the above experiments.

To deeper understand the enhanced $E_{a,i}$, we analyze the incorporation effect on the electronic structures and the chemical bonds in CsPbBr$_3$. **Figure 4**a shows the metal ion incorporated CsPbBr$_3$ supercell with $3 \times 3 \times 3$ k-mesh used for study. Note that the Cs is not shown for simplification reason. The supercell contains three crystallography nonequivalent Pb-Br octahedrons denpending on their distance to the metal ion dopant, which are highlighted in the figure. The crystallography nonequivalent Pb—Br bonds in the three octahedrons are also indicated. For chemical bonding investigation, we use the LOBSTER program to calculate the projected crystal orbital Hamilton population (pCOHP).[44–46] As a representative, Figure 4b shows the local density of states (DOSs) and the corresponding –pCOHP for the pure Pb—Br and Ni—Br$_3$ bonds and the Pb$_1$—Br$_3$, Pb$_1$—Br$_2$, and Pb$_1$—Br$_1$ bonds in the Pb$_1$-Br octahedron. It is seen that both the valence band and conduction band edges are antibonding, as indicated by the negative –pCOHP values. The integrated –pCOHP (IpCOHP) below the Fermi level and the corresponding bond length are shown in Figure 4c. The more negative the IpCOHP value, the fewer the antibonding states, and the stronger the bond strength. It is seen that the Mn and Ni doping are more effective in reducing the antibonding states than the Zn and Bi doping. The Ni-Br$_3$, Mn-Br$_3$, and Pb$_{1,2,3}$-Br (except Pb$_1$—Br$_3$) bonds are all stronger than the pure Pb—Br bond, whereas the Zn-Br$_3$, Bi-Br$_3$, and most of Pb$_{1,2,3}$—Br bonds are weaker than the pure Pb—Br bond. We take the Ni-incorporated Pb$_1$-Br octahedron for detailed discussions. The Ni—Br$_3$ bond has the shortest bond length (2.66 Å) and the highest bond strength (–3.91 eV) among the chemical bonds investigated, and it is 0.59 eV stronger than the pure Pb—Br bond (–3.32 eV) with a bond length of 2.999 Å. The Pb$_1$—Br$_2$ bond is slightly shorter than the pure Pb—Br bond (2.97 Å versus 2.999 Å), and it is 0.18 eV stronger than the pure Pb—Br bond. The Pb$_1$—Br$_3$ and Pb$_1$—Br$_1$ bonds are longer than the pure Pb—Br bond, which are 3.249 and 3.045 Å, respectively. Unexpectedly, the Pb$_1$—Br$_3$ bond strength shows only a slight decrease to –3.23 eV, and the Pb$_1$—Br$_1$ bond strength presents an anomalous increase to –3.41 eV. Moreover, the bond strength is observed to increase in the sequence of Pb$_1$-Br$_1$, Pb$_2$-Br$_2$, and Ni-Br$_3$, that is, the closer the V_{Br} moves to the Ni, the more the energy required for the V_{Br} migration to break the chemical bonds, explicitly explaining the increased E_{gs} and $E_{a,i}$ as shown in Figure 3b.

The pCOHP results clearly indicate that the Ni and Mn incorporation can cause a long-range lattice stabilization by reducing the antibonding states in the surrounding chemical bonds. To explore the fundamental mechanism, we investigate the projected DOSs in metal ion-incorporated Pb$_1$-Br octahedron. It is

seen in **Figure 5**a that in pure Pb—Br bond, the antibonding states at valence band edge are formed by the coupling between fully-filled Pb 6s orbital containing one lone-pair electron and Br 4p orbital. It is well known that the formation of such antibonding states is key to many of the appealing properties of halide perovskites such as defect tolerance, but it also weakens chemical bonds and leads to lattice instability.[2] For Mn- and Ni-doped cases, the projected DOSs shown in Figure 5b,c reveal that there is hybridization between the Ni and Mn 3d, Pb 6s, and Br 4p orbitals. Namely, the Mn and Ni 3d orbitals are coupling with the Pb 6s-Br 4p antibonding states. Such a coupling facilitates transfer of the lone-pair electron in the Pb-Br octahedrons to the partially-filled Mn and Ni 3d orbitals via coordination effect and passivates the active antibonding states, leading to the enhancement of the bond strength as reported in Figure 4c. However, as shown in Figure 5d, no coupling between the Zn 3d orbital and the Pb 6s-Br 4p antibonding states is observed in the Zn doping case, because the Zn 3d orbital is fully filled and locates far away from the valence band edges. Bi^{3+} ion has electronic structure [Xe]4f^{14}5d^{10}6s^2 and possesses one 6s^2 lone-pair electron, same as the Pb^{2+} ion. It is seen in Figure 5e that the Bi 6s^2 lone-pair electron has strong antibonding coupling with the Br 4p orbital. As a result, the Bi doping increases the antibonding states instead of reducing them, as evidenced by the increased IpCOHP values shown in Figure 4c. These projected DOSs results explain why the Mn and Ni doping are efficient in suppressing ionic migration while the Zn and Bi doping are not, as observed in Figure 2e.

2.4. Substantial Suppression of Emission Color Variation

Mixed-halogen LHPs are attractive for applications in electroluminescence devices because of the easy tuning of the optical bandgap by altering the halogen composition. However, mixed-halogen LHPs usually encounter halogen segregation problems due to field-driven ionic migration,[4,5,8] which leads to bandgap shifts and thus color instability issues. We next investigate the potential of the TM incorporation strategy in addressing these issues. We take Ni-incorporated CsPbBr$_{1.5}$I$_{1.5}$ quantum dots (CsPb$_{1-x}$Ni$_x$Br$_{1.5}$I$_{1.5}$) as a study example. The device structure and the measurement scheme are the same as those depicted in Figure S2, Supporting Information. A constant electric field with a magnitude of 10 V is applied between the electrodes throughout the measurement, and the PL spectra excited by a 405-nm laser are recorded every 2 min at room temperature. The laser is immediately turned-off once each PL spectrum recording is finished (the duration of the PL recording is less than 10 s). **Figure 6**a shows the evolution of the representative PL spectra over time in pure CsPbBr$_{1.5}$I$_{1.5}$ ($x = 0$). At first, the PL spectrum shows only one peak at ≈587 nm (peak 1). Peak 1 is red-shifted to 610 nm as the measurement time increases to 4 min, accompanied by a significantly broadened spectrum width. As the measurement time further increases, two additional peaks, one at ≈521 nm (peak 2) and the other at ≈667 nm (peak 3), appear successively, and the spectrum width broadening becomes more and more pronounced. The locations of peak 2 and peak 3 are very close to the emission of pure CsPbBr$_3$ and CsPbI$_3$, respectively (Figure 1e and ref. [47]).
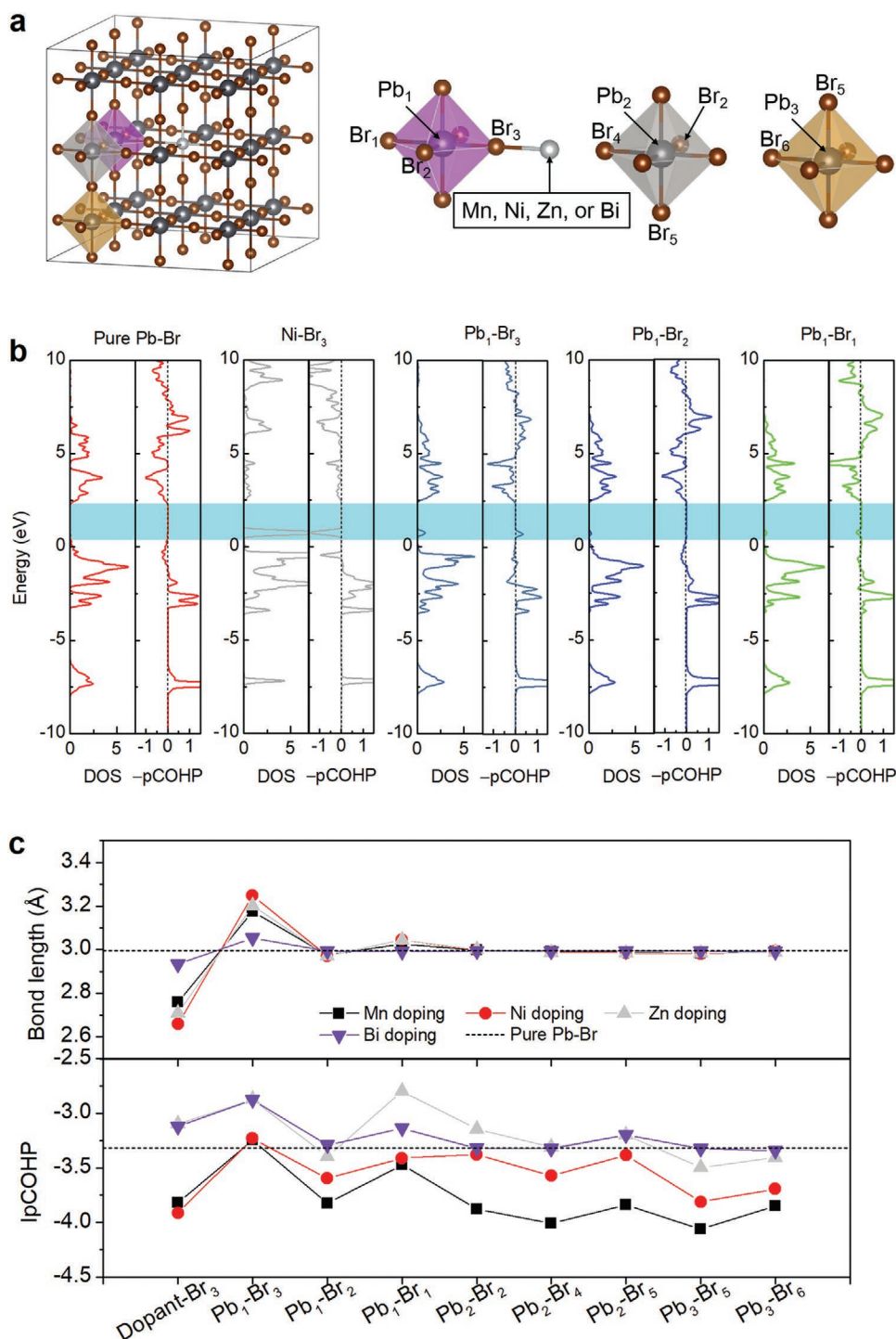
Figure 4. Chemical bonding analyses. a) The metal ion-incorpated $3 \times 3 \times 3$ CsPbBr$_3$ supercell for the pCOHP calculations. Cs is not shown in the supercell. Three crystallography nonequivalent Pb-Br octahedrons are highlighted. The crystallography nonequivalent Br ions in the three octahedrons are marked as Br$_n$ ($n = 1, 2, 3, 4, 5,$ and 6). b) Local DOSs and corresponding –pCOHP for Pb—Br bond in pure CsPbBr$_3$ and Ni—Br$_3$, Pb$_1$—Br$_3$, Pb$_1$—Br$_2$, Pb$_1$—Br$_1$ bonds in Ni-incorporated Pb$_1$-Br octahedron. c) IpCOHP and bond length for the chemical bonds as marked in (a).

Therefore, the appearance of peak 2 and peak 3 confirms an intense field-driven halogen segregation, which decomposes the CsPbBr$_{1.5}$I$_{1.5}$ film into Br-rich and I-rich regimes.

When Ni is introduced, as shown in Figure 6b,c, both the PL peak splitting and the spectrum width broadening can be

greatly suppressed. For example, in the case of $x = 0.0289$, peak 1, which is initially located at 602 nm, is slightly red-shifted to 610 nm with the measurement time increasing to 4 min. Additionally, only one weak additional peak at 515 nm (peak 2), which corresponds to the Br-rich regime, appears during the

**ADVANCED
SCIENCE NEWS**

www.advancedsciencenews.com

**ADVANCED
FUNCTIONAL
MATERIALS**

www.afm-journal.de
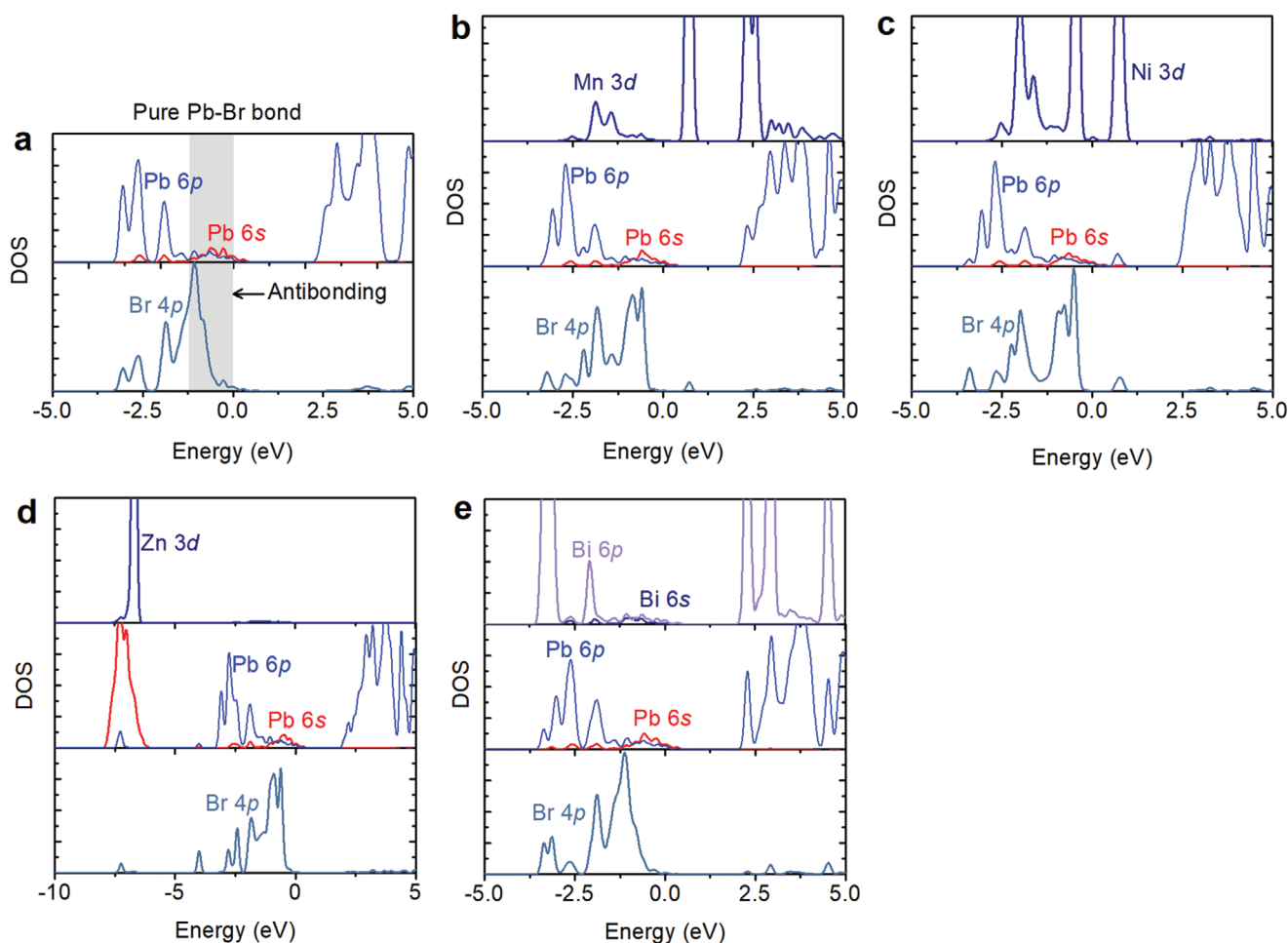
Figure 5. Electronic structure analyses. (a,b,c,d, and e) show the projected DOSs for pure Pb—Br bond and Mn-, Ni-, Zn-, and Bi-incorporated Pb_1-Br octahedron, respectively. The gray pattern in (a) indicates the energy range of the antibonding states.

whole measurement. These results indicate that the field-driven halogen segregation is inhibited by the Ni incorporation.

The Ni incorporation-induced lattice stabilization can also be seen in the change of the PL intensity with the measurement time. Figure 6d shows the intensities of peak 1, peak 2, and peak 3 (normalized to 0 min) as a function of measurement time. It is seen that the intensity of peak 1 in pure $CsPbBr_{1.5}I_{1.5}$ dramatically increases by nearly two times in the beginning and then decays exponentially to the initial value of 58% after 300 min. The PL enhancement at the very beginning of the measurement can be associated with the field-driven I^- ion redistribution that reduces the density of the electronic trap states.[48] The subsequent long-time decay is attributed to the serious halogen segregation that creates mass non-radiative recombination centers. The intensity of peak 3 in pure $CsPbBr_{1.5}I_{1.5}$ also shows dramatical change with measurement time. It increases 13 times in the beginning, followed by a long-time exponential decay. When Ni is introduced, in sharp contrast, the PL intensity variation with the measurement time becomes much more moderate due to suppressed halogen segregation. Initial sharp PL enhancement is absent. The intensity of peak 1 for $x = 0.0157$ and 0.0289 stays at 51% and 75% of the initial value at the measurement time of 300 min, respectively.

The Ni incorporation also greatly decelerates the increase of the intensity of peak 2 over time.

Figure 6e plots the Commission Internationale de l'Eclairage (CIE) 1931 chromaticity diagram determined by the measured PL spectra. It is clear that the chromaticity coordinates in the Ni-incorporated samples are much less variational than those in pure $CsPbBr_{1.5}I_{1.5}$. To quantify the Ni incorporation effect on the emission color stability, we calculate the integrated areas encircled by the chromaticity coordinate trajectory. The emission color variabilities for $x = 0$, 0.0157, and 0.0289 are estimated to be 24%, 4%, and 4% of the standard red, green, and blue (sRGB) color space, respectively, showing a sixfold reduction with the Ni incorporation. These results demonstrate that the Ni incorporation is an effective strategy for suppressing the field-driven halogen segregation and improving the operating stability in mixed-halogen LHPs.

3. Conclusion

We have reported significant ionic migration suppression and lattice stabilization in solution-processed LHP quantum dots by incorporating Ni and Mn into the Pb sites. We obtain a fourfold increase of the ionic migration energy barrier in $CsPbBr_3$ and
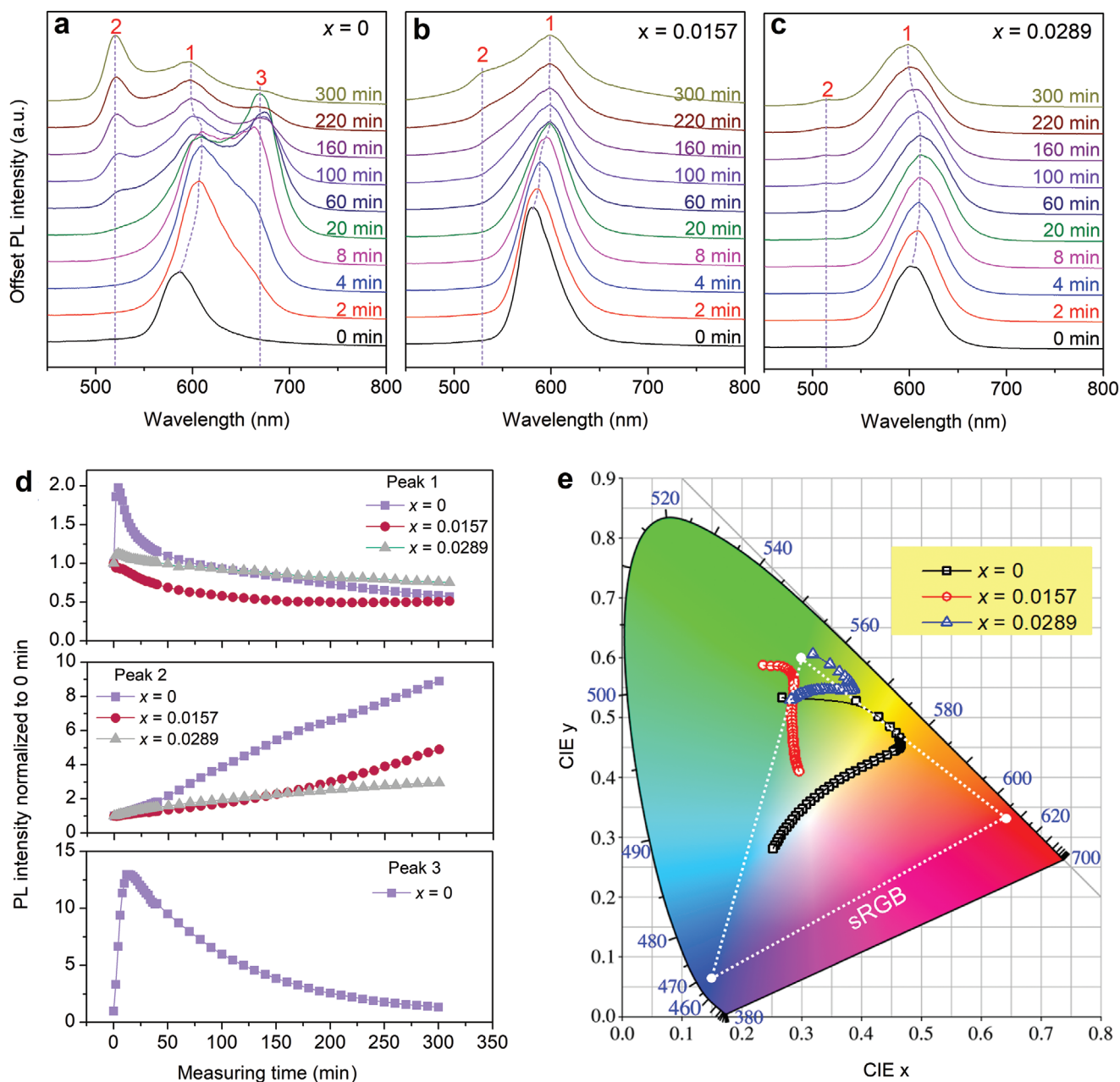
Figure 6. Suppression of emission color variation in Ni-doped $CsPbBr_{1.5}I_{1.5}$. Evolution of representative PL spectra with measurement time from 0 to 300 min in lateral devices consisting of mixed-halogen $CsPb_{1-x}Ni_xBr_{1.5}I_{1.5}$: a) $x = 0$, b) $x = 0.0157$, c) $x = 0.0289$. d) Measurement time dependence of PL intensity (normalized to that at 0 min) for different x values. The PL intensities are extracted from peak 1, peak 2, and peak 3 as labeled in (a). e) CIE 1931 chromaticity diagram for different x values. The dashed white triangle shows the sRGB color space.

a sixfold reduction of the field-driven emission color variation in $CsPbBr_{1.5}I_{1.5}$ due to greatly suppressed halogen segregation, making such a TM incorporation strategy useful for developing operationally stable LHP-based optoelectronic and electronic devices. We have also reported low efficiency of post-TM Zn and non-TM Bi incorporation in ionic migration suppression. The theoretical calculations highlight the important role of the coupling between partially-filled 3d orbital and Pb 6s-Br 4p antibonding states for efficient ionic migration suppression. The coupling can passivate the active Pb $6s^2$ lone-pair electron

and enhance the chemical bond strength in surrounding Pb-Br octahedrons, leading to long-range lattice stabilization and thus inoic migration suppression. The results also help to improve the understanding of the previously observed doping-enhanced environmental and operational stability in LHPs.

4. Experimental Section

Materials: Lead iodide (PbI_2, 99.9%), Lead bromide ($PbBr_2$, 99.99%), Bismuth bromide ($BiBr_3$, 99.9%), Manganese acetylacetonate

[Mn(acac)$_2$, 97%], Nickel acetylacetonate [Ni(acac)$_2$, 96%], Zinc acetylacetonate [Zn(acac)$_2$, 98%], and 1-octadecene (ODE, 90%) were purchased from Macklin. Cs$_2$CO$_3$ (99.99%), Oleylamine (OAm, 90%), oleic acid (OA, 85%), and ethyl acetate (99%) were purchased from Aladdin. Hexane (99.0%), Acetone (99.5%), Toluene (99.5%) was purchased from Sinopharm Chemical Reagent Corp., China. All materials were used without further purification.

Preparation of Cs-Oleate Precursor: 0.36 g Cs$_2$CO$_3$, 1.5 mL OA, and 15 mL ODE were loaded into a 100 mL three-neck flask, and the mixed solution was heated up to 120 °C after the conventional degassing and purging procedures. Thereafter, the mixture was heated to 150 °C until the solid was completely dissolved. Then, the mixture was cooled to 110 °C for further use.

Synthesis of Metal Ion-Incorporated LHPs via Hot-Injection: The metal ion-incorporated CsPbBr$_3$ quantum dots were synthesized according to hot-injection published by Kovalenko et al.[47] Here Ni-incorporated CsPbBr$_3$ was taken for illustration. 0.2 g PbBr$_2$, Ni(acac)$_2$ at a designated Ni/Pb molar ratio from 0 to 2, 15 mL ODE, 1.5 mL OA, and 1.5 mL OAm were loaded into a three-neck flask and dried under vacuum for 1 h at 120 °C. Then, the temperature was raised to 170 °C and 1.5 mL and the Cs-oleate precursor solution was injected quickly. After reacting for 5 s, the resulting mixture was cooled rapidly by immersing the flask in ice. The as-prepared quantum dots were purified based on repeated precipitation/redissolution with hexane/acetone and finally redispersed in hexane/toluene.

For the synthesis of Ni-doped CsPbBr$_{1.5}$I$_{1.5}$ quantum dots, 0.1 g PbBr$_2$, 0.1256 g PbI$_2$, 15 mL ODE, 1.5 mL OA, 1.5 mL OAm, and Ni(acac)$_2$ at a designated Ni/Pb molar ratio from 0 to 2 were added into a 100 mL three-necked flask for reaction. The other synthesis steps were similar to that of CsPbBr$_3$ described above, except that ethyl acetate instead of acetone was used for purification.

Structural and Optical Characterizations: XRD patterns were obtained by Bruker-AXS D8 Advance diffractometer with Cu Kα radiation (λ = 1.5418 Å). PL spectra were recorded using a spectrophotometer (QE65 Pro, Ocean Optics). Absolute PLQY was measured via an integrating sphere (C11347-11, Hamamatsu Photonics). The x values in CsPb$_{1-x}$TM$_x$Br$_3$ quantum dots were determined with an inductively coupled plasma mass spectrometry (iCAP TQ, Thermo Scientific). TEM images and elemental mapping were obtained by FEI Tecnai G20 equipped with energy dispersive spectrometer. The operating voltage was 200 keV. The Ni K-edge XAFS was collected at the beamline 1W1B of Beijing Synchrotron Radiation Facility in a fluorescence mode. The electrical measurements were performed by using a semiconductor analyzer (Keysight B1500A).

Device Fabrication and Measurement: Cr (10 nm)/Au (50 nm) electrodes with a distance of 20 μm were made on quartz substrates by photolithography and magnetron sputtering. The devices were fabricated by depositing the LHP quantum dots onto the Cr/Au electrodes via spin-coating, followed by annealing at 50 °C for 2 min in a vacuum drying oven to improve the contact between the quantum dots and the electrodes. The obtained devices were placed in a helium-cooling Janis cryostat (Model CCS-400H/204N) with a vacuum of $\approx 2 \times 10^{-2}$ Pa. Semiconductor analyzer (Keysight B1500A) was used for voltage source and electrical current measurement. The electrical current was detected within 0.1 s after the voltage was applied. The voltage was immediately turned off after finishing the electrical current detection.

Computational Details: The first-principles DFT calculations were performed using the Vienna ab initio simulation package (VASP).[49,50] The projector-augmented wave (PAW) method was used for describing the core-valence interaction.[51] The generalized gradient approximation of Perdew–Burke–Ernzerhof (GGA-PBE) was employed. A $3 \times 3 \times 3$ cubic-phase CsPbBr$_3$ supercell containing 135 atoms was used for the ionic migration and electronic structure calculations.[52] A kinetic energy cutoff of 350 eV was set on a grid of $3 \times 3 \times 3$ k-points. The lattice was relaxed until the force on each atom was <0.01 eV Å^{-1}. A climbing image nudged elastic band (CI-NEB) method was used for finding the transition states and the minimum energy paths.[53] Spin-orbit coupling was not included in the calculations.

Supporting Information

Supporting Information is available from the Wiley Online Library or from the author.

Conflict of Interest

The authors declare no conflict of interest.

Data Availability Statement

The data that support the findings of this study are available from the corresponding author upon reasonable request.

[1] M. V. Kovalenko, L. Protesescu, M. I. Bodnarchuk, *Science* **2017**, *358*, 745.

[2] J. Kang, L.-W. Wang, *J. Phys. Chem. Lett.* **2017**, *8*, 489.

[3] Y. Zhou, Y. Zhao, *Energy Environ. Sci.* **2019**, *12*, 1495.

[4] H. Zhang, X. Fu, Y. Tang, H. Wang, C. Zhang, W. W. Yu, X. Wang, Y. Zhang, M. Xiao, *Nat. Commun.* **2019**, *10*, 1088.

[5] X. Wang, X. Ling, X. Lian, Y. Xin, K. B. Dhungana, F. Perez-Orive, J. Knox, Z. Chen, Y. Zhou, D. Beery, K. Hanson, J. Shi, S. Lin, H. Gao, *Nat. Commun.* **2019**, *10*, 695.

[6] D. Wei, F. Ma, R. Wang, S. Dou, P. Cui, H. Huang, J. Ji, E. Jia, X. Jia, S. Sajid, A. M. Elseman, L. Chu, Y. Li, B. Jiang, J. Qiao, Y. Yuan, M. Li, *Adv. Mater.* **2018**, *30*, 1707583.

[7] J.-P. Correa-Baena, S.-H. Turren-Cruz, W. Tress, A. Hagfeldt, C. Aranda, L. Shooshtari, J. Bisquert, A. Guerrero, *ACS Energy Lett.* **2017**, *2*, 681.

[8] P. Vashishtha, J. E. Halpert, *Chem. Mater.* **2017**, *29*, 5965.

[9] H. J. Snaith, A. Abate, J. M. Ball, G. E. Eperon, T. Leijtens, N. K. Noel, S. D. Stranks, J. T.-W. Wang, K. Wojciechowski, W. Zhang, *J. Phys. Chem. Lett.* **2014**, *5*, 1511.

[10] G. Richardson, S. E. J. O'Kane, R. G. Niemann, T. A. Peltola, J. M. Foster, P. J. Cameron, A. B. Walker, *Energy Environ. Sci.* **2016**, *9*, 1476.

[11] S. Meloni, T. Moehl, W. Tress, M. Franckevičius, M. Saliba, Y. H. Lee, P. Gao, M. K. Nazeeruddin, S. M. Zakeeruddin, U. Rothlisberger, M. Graetzel, *Nat. Commun.* **2016**, *7*, 10334.

[12] J. J. Yoo, G. Seo, M. R. Chua, T. G. Park, Y. Lu, F. Rotermund, Y.-K. Kim, C. S. Moon, N. J. Jeon, J.-P. Correa-Baena, V. Bulović, S. S. Shin, M. G. Bawendi, J. Seo, *Nature* **2021**, *590*, 587.

[13] Y. Cao, N. Wang, H. Tian, J. Guo, Y. Wei, H. Chen, Y. Miao, W. Zou, K. Pan, Y. He, H. Cao, Y. Ke, M. Xu, Y. Wang, M. Yang, K. Du, Z. Fu, D. Kong, D. Dai, Y. Jin, G. Li, H. Li, Q. Peng, J. Wang, W. Huang, *Nature* **2018**, *562*, 249.

[14] K. Lin, J. Xing, L. N. Quan, F. Pelayo García de Arquer, X. Gong, J. Lu, L. Xie, W. Zhao, D. Zhang, C. Yan, W. Li, X. Liu, Y. Lu, J. Kirman, E. H. Sargent, Q. Xiong, Z. Wei, *Nature* **2018**, *562*, 245.

[15] Z. Huang, A. H. Proppe, H. Tan, M. I. Saidaminov, F. Tan, A. Mei, C.-S. Tan, M. Wei, Y. Hou, H. Han, S. O. Kelley, E. H. Sargent, *ACS Energy Lett.* **2019**, *4*, 1521.

[16] S. Wu, R. Chen, S. Zhang, B. H. Babu, Y. Yue, H. Zhu, Z. Yang, C. Chen, W. Chen, Y. Huang, S. Fang, T. Liu, L. Han, W. Chen, *Nat. Commun.* **2019**, *10*, 1161.

[17] S. Yang, S. Chen, E. Mosconi, Y. Fang, X. Xiao, C. Wang, Y. Zhou, Z. Yu, J. Zhao, Y. Gao, F. De Angelis, J. Huang, *Science* **2019**, *365*, 473.

[18] Q. He, M. Worku, L. Xu, C. Zhou, S. Lteif, J. B. Schlenoff, B. Ma, *J. Mater. Chem. A* **2020**, *8*, 2039.

[19] Y. Shao, Y. Fang, T. Li, Q. Wang, Q. Dong, Y. Deng, Y. Yuan, H. Wei, M. Wang, A. Gruverman, J. Shield, J. Huang, *Energy Environ. Sci.* **2016**, *9*, 1752.

[20] Y. Huang, L. Li, Z. Liu, H. Jiao, Y. He, X. Wang, R. Zhu, D. Wang, J. Sun, Q. Chen, H. Zhou, *J. Mater. Chem. A* **2017**, *5*, 8537.

[21] W. Zhou, Y. Zhao, X. Zhou, R. Fu, Q. Li, Y. Zhao, K. Liu, D. Yu, Q. Zhao, *J. Phys. Chem. Lett.* **2017**, *8*, 4122.

[22] N. Li, L. Song, Y. Jia, Y. Dong, F. Xie, L. Wang, S. Tao, N. Zhao, *Adv. Mater.* **2020**, *32*, 1907786.

[23] D. Lin, T. Shi, H. Xie, F. Wan, X. Ren, K. Liu, Y. Zhao, L. Ke, Y. Lin, Y. Gao, X. Xu, W. Xie, P. Liu, Y. Yuan, *Adv. Energy Mater.* **2021**, *11*, 2002552.

[24] M. Pazokia, M. J. Wolf, T. Edvinsson, J. Kullgren, *Nano Energy* **2017**, *38*, 537.

[25] S. Hou, M. K. Gangishetty, Q. Quan, D. N. Congreve, *Joule* **2018**, *2*, 2421.

[26] M. K. Gangishetty, S. N. Sanders, D. N. Congreve, *ACS Photonics* **2019**, *6*, 1111.

[27] Y. Ji, J.-B. Zhang, H.-R. Shen, Z. Su, H. Cui, T. Lan, J.-Q. Wang, Y.-H. Chen, L. Liu, K. Cao, W. Shen, S. Chen, *ACS Omega* **2021**, *6*, 13831.

[28] X. Gong, L. Guan, H. Pan, Q. Sun, X. Zhao, H. Li, H. Pan, Y. Shen, Y. Shao, L. Sun, Z. Cui, L. Ding, M. Wang, *Adv. Funct. Mater.* **2018**, *28*, 1804286.

[29] Z.-J. Yong, S.-Q. Guo, J.-P. Ma, J.-Y. Zhang, Z.-Y. Li, Y.-M. Chen, B.-B. Zhang, Y. Zhou, J. Shu, J.-L. Gu, L.-R. Zheng, O. M. Bakr, H.-T. Sun, *J. Am. Chem. Soc.* **2018**, *140*, 9942.

[30] L. Chen, L. Wan, X. Li, W. Zhang, S. Fu, Y. Wang, S. Li, H.-Q. Wang, W. Song, J. Fang, *Chem. Mater.* **2019**, *31*, 9032.

[31] G. Pan, X. Bai, W. Xu, X. Chen, Y. Zhai, J. Zhu, H. Shao, N. Ding, L. Xu, B. Dong, Y. Mao, H. Song, *ACS Appl. Mater. Interfaces* **2020**, *12*, 14195.

[32] M. I. Saidaminov, J. Kim, A. Jain, R. Quintero-Bermudez, H. Tan, G. Long, F. Tan, A. Johnston, Y. Zhao, O. Voznyy, E. H. Sargent, *Nat. Energy* **2018**, *3*, 648.

[33] C. Bi, X. Sun, X. Huang, S. Wang, J. Yuan, J. X. Wang, T. Pullerits, J. Tian, *Chem. Mater.* **2020**, *32*, 6105.

[34] W. Xu, L. Zheng, X. Zhang, Y. Cao, T. Meng, D. Wu, L. Liu, W. Hu, X. Gong, *Adv. Energy Mater.* **2018**, *8*, 1703178.

[35] X. Shai, L. Zuo, P. Sun, P. Liao, W. Huang, E.-P. Yao, H. Li, S. Liu, Y. Shen, Y. Yang, M. Wang, *Nano Energy* **2017**, *36*, 213.

[36] J. J. Rehr, R. C. Albers, *Rev. Mod. Phys.* **2000**, *72*, 621.

[37] J. Pena, K. D. Kwon, K. Refson, J. R. Bargar, G. Sposito, *Geochim. Cosmochim. Acta* **2010**, *74*, 3076.

[38] I. E. Castelli, J. M. Garcia-Lastra, K. S. Thygesen, K. W. Jacobsen, *APL Mater.* **2014**, *2*, 081514.

[39] J. Mizusaki, K. Arai, K. Fueki, *Solid State Ionics* **1983**, *11*, 203.

[40] C. Eames, J. M. Frost, P. R. F. Barnes, B. C. O'Regan, A. Walsh, M. S. Islam, *Nat. Commun.* **2015**, *6*, 7497.

[41] K. Miyata, D. Meggiolaro, M. T. Trinh, P. P. Joshi, E. Mosconi, S. C. Jones, F. De Angelis, X.-Y. Zhu, *Sci. Adv.* **2017**, *3*, e1701217.

[42] L. Jin, Y. Qian, Y. Zhang, M. Bowen, S. Ding, *J. Mater. Sci.: Mater. Electron.* **2020**, *31*, 1945.

[43] G. Huang, C. Wang, S. Xu, S. Zong, J. Lu, Z. Wang, C. Lu, Y. Cui, *Adv. Mater.* **2017**, *29*, 1700095.

[44] R. Dronskowski, P. E. Blöchl, *J. Phys. Chem.* **1993**, *97*, 8617.

[45] V. L. Deringer, A. L. Tchougreeff, R. Dronskowski, *J. Phys. Chem. A* **2011**, *115*, 5461.

[46] S. Maintz, V. L. Deringer, A. L. Tchougreeff, R. Dronskowski, *J. Comput. Chem.* **2013**, *34*, 2557.

[47] L. Protesescu, S. Yakunin, M. I. Bodnarchuk, F. Krieg, R. Caputo, C. H. Hendon, R. X. Yang, A. Walsh, M. V. Kovalenko, *Nano Lett.* **2015**, *15*, 3692.

[48] D. W. deQuilettes, W. Zhang, V. M. Burlakov, D. J. Graham, T. Leijtens, A. Osherov, V. Bulović, H. J. Snaith, D. S. Ginger, S. D. Stranks, *Nat. Commun.* **2016**, *7*, 11683.

[49] G. Kresse, J. Hafner, *Phys. Rev. B* **1993**, *47*, 558.

[50] G. Kresse, J. Furthmüller, *Phys. Rev. B* **1996**, *54*, 11169.

[51] G. Kresse, D. Joubert, *Phys. Rev. B* **1999**, *59*, 1758.

[52] J. P. Perdew, K. Burke, M. Ernzerhof, *Phys. Rev. Lett.* **1996**, *77*, 3865.

[53] G. Henkelman, B. P. Uberuaga, H. Jónsson, *J. Chem. Phys.* **2000**, *113*, 9901.